Pattern Formation Framework for Chimera States in Complex Networks

Malbor Asllani
*Department of Mathematics, Florida State University, 1017 Academic Way, Tallahassee, FL 32306, United States of America**

Alex Arenas
Departament d'Enginyeria Informàtica i Matemàtiques, Universitat Rovira i Virgili, 43007 Tarragona, Spain and Pacific Northwest National Laboratory, 902 Battelle Blvd, Richland, WA, 99354, USA†

(Dated: March 25, 2025)

Chimera states, marked by the coexistence of order and disorder in systems of coupled oscillators, have captivated researchers with their existence and intricate patterns. Despite ongoing advances, a fully understanding of the genesis of chimera states remains challenging. This work formalizes a systematic method by evoking pattern formation theory to explain the emergence of chimera states in complex networks, in a similar way to how Turing patterns are produced. Employing linear stability analysis and the spectral properties of complex networks, we show that the randomness of network topology, as reflected in the localization of the graph Laplacian eigenvectors, determines the emergence of chimera patterns, underscoring the critical role of network structure. In particular, this approach explains how amplitude and phase chimeras arise separately and explores whether phase chimeras can be chaotic or not. Our findings suggest that chimeras result from the interplay between local and global dynamics at different time scales. Validated through simulations and empirical network analyses, our method enriches the understanding of coupled oscillator dynamics.

I. INTRODUCTION

Complex networks are crucial for examining complex systems in both natural and synthetic settings [1]. They are particularly instrumental to understand how different interconnected components within a system interact to manifest collective behaviors. One of the most fascinating collective phenomena observed in complex networks is the synchronization of oscillators, where individual components, despite their diverse functions and environments, achieve coherent oscillations [2–5]. Synchronization occurs in many natural and engineered settings, from neurons in the brain coordinating actions [6, 7] and fireflies synchronously flashing for mating [8], to power grids where it ensures stability [9], and communication networks where it prevents data loss and enhances efficiency [10]. In the realm of synchronization, the concept of chimera states—where coherent and incoherent oscillators coexist—represents a significant theoretical challenge and has been a focus of extensive research [11–23]. These states illustrate a striking blend of order and disorder within networked systems, where order is understood as amplitude coherence, or both amplitude and phase coherence. Chimera states have been found to be stable in infinite-size networks [24] and transient in finite ones [25]. Nevertheless, rigorous results have been obtained in weak chimeras, defined as a type of invariant set exhibiting partial frequency synchronization [26, 27]. Of particular relevance to this paper is the formulation of chimera states in diffusively coupled amplitude-phase oscillators, moving beyond the reductionist approach of phase-only models and extending the analysis to more realistic settings. Recent contributions in this direction include *amplitude chimeras*, where the amplitude exhibits incoherence while the phase remains coherent [14]; *amplitude-mediated chimeras*, where amplitude variations influence phase dynamics, leading to the coexistence of coherence and incoherence in both amplitude and phase [28, 29]; and *strong chimeras*, which are permanently stable, have an identically synchronized coherent domain, and do not co-occur with stable global synchronization [30, 31]. In particular, the latter arises during the transition from a globally coherent to a globally incoherent state as a bifurcation parameter varies, a feature similar to what is analyzed in this paper.

Despite numerous studies, complete explanations for their stability and emergence are still sought [13]. Experimental studies have definitively confirmed the relevance of chimera states in various human-made setups: chemical oscillators using the Belousov–Zhabotinsky reaction with light feedback [32, 33], optical systems with spatial light modulators [34], mechanically coupled metronomes on swings [35], and photoelectrochemical experiments modeling silicon oxidation [36]. Furthermore, observations in both neuroscience and ecology suggest their occurrence in natural settings: in the human brain, chimera states manifest as patterns of partial synchrony among brain regions fundamental to cognitive organization [37], while in ecology, video recordings of *Photuris frontalis* fireflies reveal spontaneous, stable chimera states where groups within a swarm flash synchronously but with a constant delay [38].

An early effort to understand chimera states [39] considered two populations of identical Kuramoto oscilla-

* masllani@fsu.edu
† alexandre.arenas@urv.cat

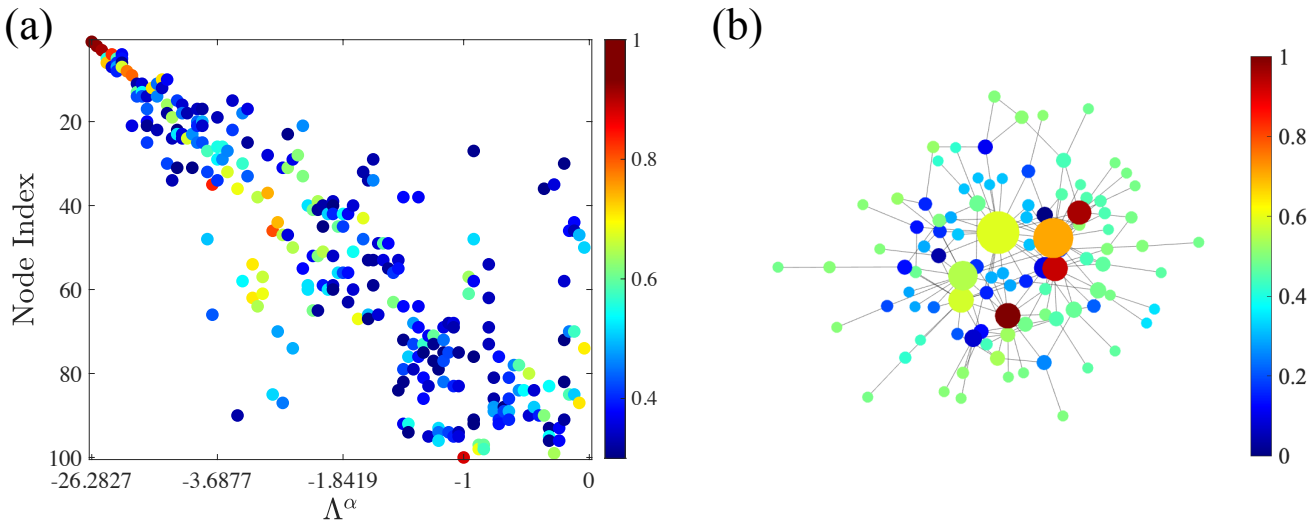

FIG. 1. **Eigenvector localization and chimera states in a Scale-Free (SF) network.** (a) The panel displays the absolute values of the matrix's eigenvectors as columns, with entries below 0.3 in magnitude omitted for clarity. (b) The normalized colormap in the network visualization provides a snapshot that illustrates the amplitude of the chimera for the Rössler model. Referring to the color code, it can be observed that peripheral nodes (those less connected) share a similar amplitude, while the disorder is localized in the central nodes (hubs). The SF network was generated with parameters $N = 100$, $m_0 = 5$, and $m = 3$ and the nodes' size represents their degree. Additionally, the nodes are labeled in decreasing degree order. The parameters for the Rössler model are $a = 0.01$, $b = 0.2$, $c = 30$, $D_\phi = D_\psi = 0$, $D_\chi = 0.2$, $\kappa = 0.02$.

tors, strongly coupled within groups and weakly between them. Later approaches aimed to partition networks into synchronized and desynchronized regions using symmetry-based methods [40] or block diagonalization techniques [31, 41]. These rely on network structure to predict coherent or incoherent dynamics. More recently, we proposed a spectral approach to indirectly identify substructures conducive to chimera emergence [42], analyzing coupled differential equations on modular networks. Our analysis showed that, via a pattern formation mechanism, it is possible to predict which modules will synchronize or desynchronize. While symmetry-breaking methods [42, 43] capture the coexistence of coherence and incoherence, they are limited by strong modularity and model-specific assumptions. Muolo *et al.* [44] extended this approach by using the triangular structure of Laplacian eigenvectors—common in many directed networks [45–48]—to localize disorder. Though promising, this method remains limited in networks with weak or no modular structure. Most studies on pattern formation in networks have focused on bifurcation conditions. Only recently have a few works [49–51] begun to explore the resulting patterns, though none address chimera states. In a related context, Sethia et al. [28, 29] demonstrated amplitude-mediated chimeras in the nonlocal complex Ginzburg–Landau equation, suggesting that different mechanisms may underlie distinct types of chimera states.

Building on these insights, our work introduces an alternative perspective aimed at enriching the broader discourse on chimera states by applying pattern formation theory to the emergence of these states. Such an approach is mathematically grounded on weakly nonlinear analysis, a technique used to study systems that are close to a linear regime but exhibit small nonlinearities, originally developed by Kuramoto [52], and later applied it also to networked systems [53–55]. Specifically, it helps determine which parts of the network will desynchronize and which will remain synchronized. The basics of weakly nonlinear analysis in this problem are as follows. First, we identify a small parameter that quantifies the strength of the nonlinearity, ensuring the system remains close to its linear regime. The system starts in a homogeneous fixed-point state, near the Hopf bifurcation threshold. A perturbation in the small parameter then induces this bifurcation, leading to global oscillatory instabilities. Second, we analyze the linearized system near the bifurcation to determine which modes become unstable. Two types of instabilities may arise depending on the system: a non-spatial (complex) mode that drives uniform node-level oscillations, and a spatial mode that, depending on whether it is real or complex, leads to stationary or oscillatory spatial patterns. The crux of this approach—following the same insights as Turing's analysis of diffusion-driven instability—is that the critical eigenfunction (or eigenvector) associated with the unstable spatial mode determines the structure of the emergent pattern at equilibrium.

Throughout this paper, for the sake of clarity and representativeness, we consider two models: the Brusselator, a set of autocatalytic reactions for two chemicals (two–species) that can exhibit complex dynamic behaviors,

which we will show is related to the real spatial mode; and the Rössler attractor, a system of three nonlinear ordinary differential equations that serves as a paradigmatic example of a chaotic system. This is a three–species model related to the complex spatial mode. Details of both models are provided in the Appendix.

The key focus of this paper is to explore how the spectral properties of networks influence the development of chimera patterns, building upon the pattern formation theory that has been developed and matured over the past five decades [56, 57]. Our insight comes from the fact that many random complex networks have strong eigenvector localization of the Laplacian matrix, i.e., the nonzero or dominant elements are concentrated in a small set of the components of the eigenvector [58–60] (see Fig. 1(a), where the Laplacian eigenvectors are represented as columns in the visualization matrix for a scale-free (SF) network [61]; see also the Appendix for details on how the network is generated).

This localization, which is similar to the eigenfunctions in solid state physics, in the presence of impurities, and known as Anderson localization [62–65], has been observed to help understand disease spreading dynamics [66]. In particular, it has been demonstrated that the localized entries correspond to a subset of nodes that share similar degrees [59]. Once one of these eigenvectors is selected as the critical one, a supercritical bifurcation ensures that the emergent phase or/and amplitude pattern will follow the same trend observed in the localization structure. Nodes with localized entries leave the synchronized manifold and change either their amplitude only, for stationary instabilities, or both the amplitude and the phase for oscillatory ones. In this paper, we will demonstrate that chimeras are structurally localized spatio-temporal patterns, as illustrated in Fig. 1(b).

The rest of the paper is structured as follows: in Section II, we briefly review key concepts from pattern formation theory that form the basis for our analysis of chimera states, with particular emphasis on the role of Laplacian eigenvectors in shaping emerging patterns. In Section III, we illustrate the application of this framework to two different dynamical systems on both real and synthetic networks. We conclude by discussing the broader implications of our findings. The full mathematical details of the perturbation analysis are provided in the Appendix.

II. PATTERN FORMATION IN COMPLEX NETWORKS

The theory of pattern formation investigates mechanisms that lead to the self-organization of complex patterns in reaction-diffusion systems. This theory provides insights into the principles underlying the spontaneous emergence of order in diverse biological and physical phenomena [56, 57]. It is based on a weakly nonlinear analysis approach that allows predicting the shape of the final nonlinear patterns [52, 56, 57]. Originally developed to explore spatially extended patterns in continuous media [56], pattern formation theory has since been adapted to complex networks, significantly enhancing our insight into the dynamics of intricate patterns within these systems [53, 54, 67–72]. In this section, we briefly summarize the pattern formation theory in a system of reaction-diffusion equations in networks of coupled identical limit-cycle oscillators, following references [53, 55]. Indeed, Kuramoto employed a pattern formation framework to derive phase-reduced equations, often approximating oscillator coupling via a continuous Laplacian operator. His analysis, particularly through the Complex Ginzburg–Landau equation, captured dynamics in both phase and amplitude near Hopf bifurcations. In our approach, we build on this foundation but retain the full amplitude–phase dynamics without applying a phase reduction. This allows us to extend the applicability of pattern formation theory to systems where amplitude variations—such as in amplitude chimeras—may play a significant role. Nonetheless, like in Kuramoto's treatment, we observe that near criticality, amplitude deviations in the emergent pattern remain negligible.

Let us start by considering a $M \times N-$dimensional reaction-diffusion system and label $\mathbf{x}_j(t)$ for $j = 1, \ldots, N$ as the M-dimensional vector representing densities of the chemical or species under consideration, where the index j refers to the node of the network. Globally, the dynamics of the system is described by the set of networked coupled differential equations.

$$\dot{\mathbf{x}}_j = \mathbf{F}(\mathbf{x}_j, \boldsymbol{\mu}) + \mathbf{D}\sum_{k=1}^{N} L_{jk}\mathbf{x}_k, \quad \forall j \tag{1}$$

where the M-dimensional vector function $\mathbf{F}$ specifies the nonlinear reaction part with $\boldsymbol{\mu}$ representing the vector of parameters. For the spatial part, diffusive coupling: $\mathbf{D} = \kappa\,\mathrm{diag}(D_1, D_2, \ldots, D_M)$ denotes the diagonal matrix of diffusion coefficients where κ is a constant parameter representing the coupling strength. The network structure is encapsulated in $\mathbf{L}$, the Laplacian kernel defined through the adjacency matrix $\mathbf{A}$ as $\mathbf{L} = \mathbf{A} - \mathbf{K}$, where $\mathbf{K}$ is the diagonal matrix of the degrees. The system (1) admits a homogeneous equilibrium point $\mathbf{x}^*$. It is also required that when only the reaction part is considered ($\kappa = 0$), $\mathbf{x}^*$ undergoes a Hopf bifurcation for $\boldsymbol{\mu} = \boldsymbol{\mu}_0$. Slightly above this threshold, $\mathbf{x}^*$ becomes unstable, and a limit cycle emerges for each node of the network in its non-spatial limit ($\kappa = 0$). The spatial coupling ($\kappa \neq 0$) is known to synchronize these limit cycles in a globally coherent synchronization across the entire network. However, if global instability conditions are fulfilled, tiny non-homogeneous perturbations can destabilize the uniform synchronous equilibrium.

We begin by introducing small inhomogeneous perturbations, $\mathbf{u}_j$, to the uniform equilibrium point, thereby slightly perturbing the system from its steady state, resulting in $\mathbf{x}_j = \mathbf{x}_j^* + \mathbf{u}_j$ for $j = 1, \ldots, N$. Substituting this into equations (1) and performing a linearization yields

the following equation for the short time evolution of $\mathbf{u}_j$:

$$\dot{\mathbf{u}}_j \approx \mathbf{J}\mathbf{u}_j + \mathbf{D}\sum_{k=1}^{N} L_{jk}\mathbf{u}_k, \tag{2}$$

where $\mathbf{J}$ is the Jacobian matrix evaluated at the steady state $\mathbf{x}^*$. Given that the Laplacian eigenvectors form an orthogonal basis, we look for solutions of the form:

$$\mathbf{u}_j = \sum_{\alpha=1}^{N} \mathbf{c}_\alpha V_j^\alpha e^{\lambda_\alpha t}, \tag{3}$$

where $\mathbf{c}_\alpha$ are M-dimensional vectors representing the coefficients for each species, V_j^α are the entries of the Laplacian eigenvectors, and λ_α are the growth rates of the perturbations, all corresponding to the eigenmode Λ^α. Substituting this solution into Eq. (2) and after some algebraic manipulation (see Appendix for details), using the eigenvalue/eigenvector property $\sum_{k=1}^{N} L_{jk}V_k^\alpha = \Lambda^\alpha V_j^\alpha$, one can establish that the growth rates λ_α are the M eigenvalues of $(\mathbf{J}+\Lambda^\alpha\mathbf{D})$. The relationship $\lambda_\alpha(\Lambda^\alpha)$, mapping the Laplacian eigenvalues Λ^α to the growth rate λ_α with the maximum real part among the M eigenvalues, is also known as the discrete dispersion relation [67, 68], analogous yet distinct from the MSF. Before proceeding further, we want to point out that, although the assumption of identical oscillators is a requirement for the dispersion relation/MSF formalism and is commonly used in the literature, it has been shown that such a framework can be extended to relax this constraint [73, 74].

As mentioned already, Eq. (3) describes the behavior of the system under scrutiny only for the initial evolution of the system near the (unstable) steady state, which in principle differs from the long-term behavior, i.e., equilibrium, where the final pattern is observed. An exception to this occurs when the parameters are set as described earlier, near the critical point and for weak spatial coupling, i.e., $\kappa \ll 1$. This regime allows for a weakly nonlinear analysis through multiple-scale perturbation theory, providing an equation to approximately describe the amplitude evolution of the perturbations, known as the Complex Ginzburg-Landau (CGL) equation. The CGL equation serves as a normal form for describing the amplitude of a pattern [75]. In this paper, we will not delve into the details of analytical/numerical approximations of equation (1), but instead, we will use the CGL formalism to validate the pattern predictions obtained through linear stability analysis. Details of the derivation of the CGL amplitude equation are given in the Appendix. Notably, the significance of the weakly nonlinear approach lies in its role as the normal form for a Hopf pitchfork bifurcation, particularly in the case of a supercritical bifurcation. For a suitable choice of parameters, the linear stability analysis of the CGL solution indicates stability in the supercritical case and instability in the subcritical case. This aligns with the specific scenario where, as predicted by perturbation theory, a small amplitude pattern is expected as operating slightly above the critical point $\boldsymbol{\mu_0}$. In the literature, it has been established that the CGL is always in the supercritical regime for the Brusselator model [55]. Additionally, we numerically demonstrate in the Appendix that this is consistently also true for the Rössler model with our selected parameters.

A. How Laplacian eigenvectors shape emerging patterns

This point is crucial and conclusive for the pattern selection process, as it reveals how structural features of the network govern the emergence and spatial organization of the pattern. The normal form, described by the Complex Ginzburg-Landau equation, reveals that near the threshold of instability, the solution of the original reaction-diffusion system (1) reaches equilibrium after a rapid saturation of the linear evolution of the perturbation, $\mathbf{u}_j$, confirming Turing's original intuition [76]. Consequently, the final pattern will take the form of the critical eigenvector (or a linear combination of such eigenvectors) established using linear stability analysis of (1) as follows:

$$\mathbf{u}_j = \sum_{\alpha\in\mathcal{U}} \mathbf{c}_\alpha V_j^\alpha e^{\lambda_\alpha t} + \sum_{\alpha\in\mathcal{S}} \mathbf{c}_\alpha V_j^\alpha e^{\lambda_\alpha t}, \tag{4}$$

where we have separated Eq.(3) in $\mathcal{U}$, the set of indices corresponding to unstable modes, and $\mathcal{S}$ the set of indices corresponding to stable modes. Note that, $\alpha = N$ corresponding to the null Laplacian eigenvalue $\Lambda^N = 0$ (the non-spatial mode) belongs to $\mathcal{U}$ since $\lambda_N = i\omega_0$.

Two scenarios arise from this analysis: (a) *stationary spatial instability*, when the critical spatial mode derived from the linear stability analysis has no imaginary part, $\Im(\lambda_\alpha) = 0\ \forall\alpha \in \mathcal{U}\setminus\{N\}$. In this case, the spatial mode contributes only to the shape of the final pattern, not to its temporal dynamics; and (b) *oscillatory instability*, when the imaginary part of at least one of the critical spatial modes is non-zero, $\exists\alpha = c \in \mathcal{U}\setminus\{N\}$ such that $\Im(\lambda_\alpha) \neq 0$. In this case, an additional temporal frequency $\omega_c = \Im(\lambda_\alpha)$ (compared to the intrinsic oscillations ω_0) is added to the dynamics of the pattern at equilibrium.

III. AMPLITUDE AND PHASE LOCALIZATION

Building on the spectral localization concepts discussed earlier in this paper, we now examine the implications of the outcomes derived from the linear stability analysis. This analysis suggests that depending on the nature of the dispersion relation introduced earlier, the system may exhibit stationary spatial instabilities, and oscillatory instabilities. Our claim is that these solutions do correspond to various types of chimera states, characterized by either amplitude or phase disorder, or both.

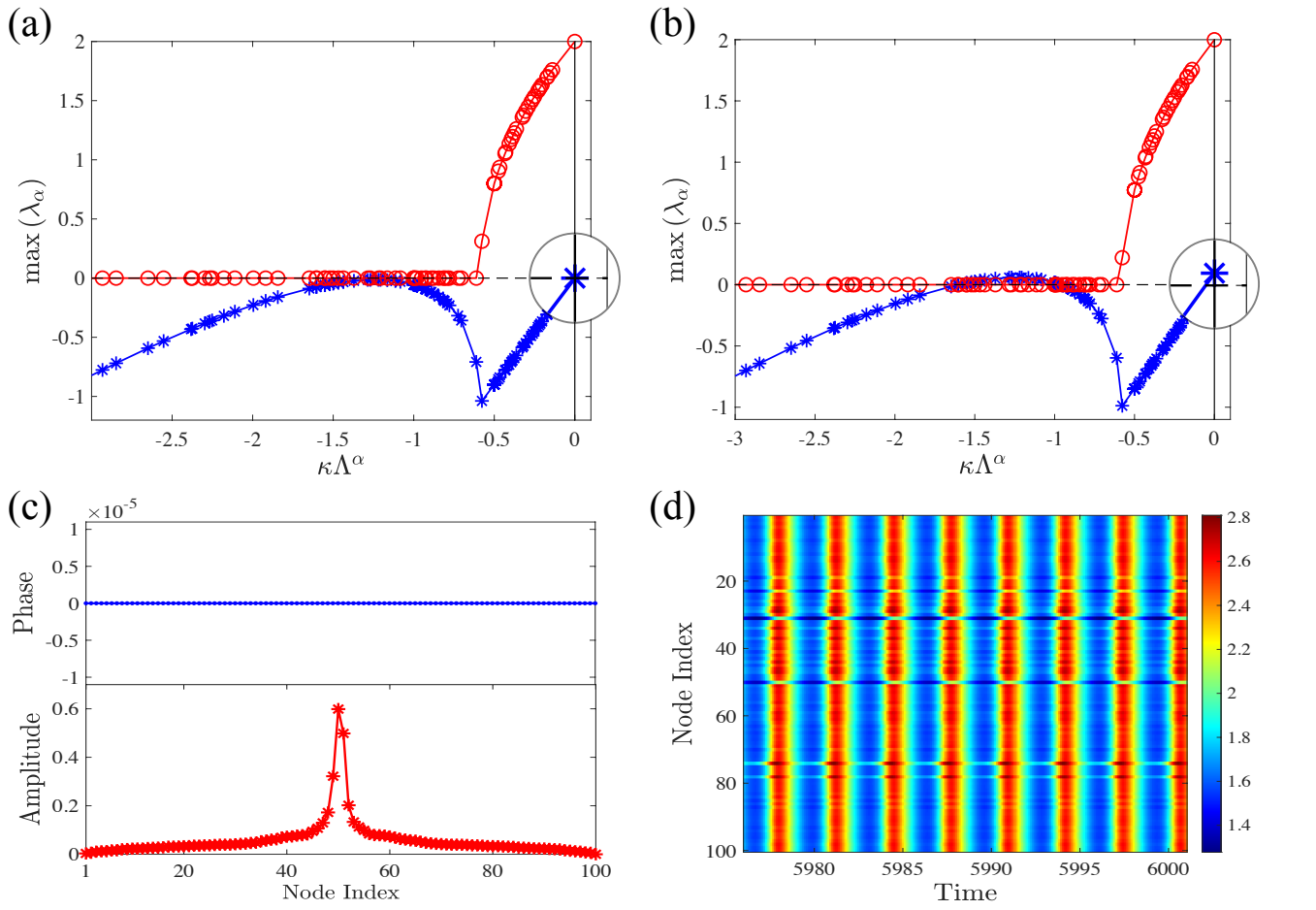

FIG. 2. **Amplitude Chimera States in the Brusselator Model.** Real (blue stars) and imaginary (red circles) parts of the dispersion relation: (a) with $b = 5$ in the pre-perturbation setting and (b) with $b = 5.1$ where chimera occurs, zoomed at the origin for clarity. (c) Phase (upper) and amplitude (lower) differences from the original limit cycle, with oscillators maintaining the same phase. To better visualize the localization of the disorder, the nodes are intentionally indexed to yield a center-peaked symmetric amplitude distribution. (d) Pattern evolution at equilibrium, showing amplitude disruptions. The remaining parameters are $a = 2$, $D_\phi = 5$, $D_\psi = 13$, and $\kappa = 0.1$, and the network used is depicted in Fig. 1.

Notably, the eigenvectors $\mathbf{V}^\alpha$, $\alpha \in \mathcal{U}$ are critical to our study, as we will show on specific examples.

We begin by considering the dispersion relation for two well-know dynamical systems in networks: the Brusselator model, and the Rössler model (see Appendix for the models' details). The Brusselator model dispersion relation is illustrated in Figure 2. They represent respectively the pre-perturbation settings Fig. 2(a) and the post-perturbation settings Fig. 2(b). It can be noticed that the Brusselator-based reaction-diffusion system exhibits a Hopf bifurcation only at the origin, identified by the presence of a non-null imaginary part (red circles), which leads to the intrinsic oscillations of the nodes.

Mathematically, this is explained by the fact that being a two-species model, the only kind of instability it can undergo at the spatial level, i.e., $\Lambda^\alpha \neq 0$, is of a stationary type where the set of eigenvalues for which the instability occurs are all strictly real [56, 57]. Our analysis predicts no traveling wave effects in this model, as the critical non-zero mode of the Laplacian is purely real. Therefore, oscillations are confined to the non-spatial mode at the origin. Consequently, the pattern governed by the localized (purely real) entries of the critical eigenvectors $\mathbf{V}^\alpha$ will display amplitude disorder at a subset of nodes while maintaining their original phase in both frequency and phase lag. This is confirmed in Fig. 2(c), where the amplitude-only chimera state is distinctly visible. The node indexing is adjusted to reflect a symmetric, *center-peaked* distribution, where phase and amplitude values reach their maximum at the center and decrease symmetrically toward the edges. For clarity and consistency throughout the paper, we will refer to this structure as "center-peaked" in our analysis and discussion. Such representation aims to better visualize the localization of amplitude and/or phase disorder by separating the synchronized from the unsynchronized oscillators on one side and offering a better comparison of the amount of disorder per node. Fig. 2(d) shows the temporal evolution of

the amplitude chimera at equilibrium.

The situation differs drastically in the Rössler model (a three-species model), where a Hopf bifurcation can occur for a spatial model different from $\Lambda^\alpha \neq 0$ [56, 57]. As anticipated earlier, such instability occurs when the non-null spatial mode of the Laplacian has a corresponding Jacobian eigenvalue in the dispersion relation with an imaginary part different from zero. This is shown in the dispersion relation of Fig. 3, where a small change in the parameters transitions the system from the state presented in Fig. 3(a) to the one in Fig. 3(b), where the modes with a positive real part (blue stars) now have a nonzero imaginary part (red circles). This mechanism, known as oscillatory instability [56], is responsible for generating traveling waves in the spatial support. The peculiar characteristics of the Rössler model, known for its oscillatory behavior—whether chaotic or not—result in all modes of the dispersion relation transitioning from stable to unstable, with a decreasing slope towards the origin as shown in Fig. 3(b). This, together with an omnipresent imaginary part in the dispersion relation, suggests that a spatially varying oscillatory pattern can be anticipated. In the parameter setting shown in Fig. 3(c), we observe how initially synchronized but chaotic states emerge, exhibiting localized amplitude disorder. Due to its small amplitude, this disorder can be considered negligible when near the instability threshold, as anticipated by Kuramoto [52]. This is understandable considering the small amplitude approach to the problem on one hand (see Appendix), and the two-speed pace of the imaginary and real parts of the dispersion relation which allows a full development of the oscillations while the amplitude develops slightly, so one can focus on the phase only. Notably, the phase behavior, as depicted in a stroboscopic plot, Fig. 3(c), shows localized chaotic incoherence within a subgroup of oscillators, maintaining an average phase difference from the originally synchronized state. As before, the indexing of nodes is adjusted to represent a center-peaked symmetric distribution for both phase and amplitude differences for a better visualization of the separation of the coherent and incoherent oscillators. However, due to the stroboscopic representation of the phase—where values are sampled at discrete intervals—a maximum in one cycle may appear as a minimum in another. The same behavior is confirmed by the temporal evolution in Fig. 3(d).

Complementary comparisons between the set of critical eigenvectors and the final pattern confirm the precise localization of the amplitude of the pattern. Figure 4(a)-(d), display snapshots of the Brusselator equilibrium pattern shown with blue circles, for different values of the coupling strength κ. These patterns are analytically reconstructed using a linear combination of the basis of the Laplacian eigenvectors, expressed as $\boldsymbol{\phi} = \sum_{\alpha=1}^{N} m_\alpha \mathbf{V}^\alpha$, where the scalar coefficients m_α have been numerically estimated. As observed in the insets, the coefficients peak at specific values (corresponding to the critical eigenvalues of their respective dispersion relations), confirming that only a few eigenvectors shape the final patterns. Additionally, there is a second peak corresponding to the origin, where the eigenvector is uniformly distributed. Importantly, the indexing of the nodes in Figure 4 remains unchanged compared to Fig. 1(a), meaning that nodes are labeled in decreasing order of their degrees. Following the portrayal of Fig. 1(a), the localization is stronger in the first eigenvectors of the Laplacian and becomes weaker as their order increases. We can control the critical eigenvector by tuning the coupling strength κ. As anticipated previously, the eigenvector localization is centered around entries that correspond to nodes with similar degrees, meaning that the amplitude disorder will localize accordingly, as shown in Fig. 4(e)-(h). To quantify the amount of localization, in Fig. 4(i) we have used the Inverse Participation Ratio (IPR), initially developed to measure the Anderson localization, defined for a non-normalized vector $\boldsymbol{\Phi}$ with components Φ_i as $\mathrm{IPR}(\boldsymbol{\Phi}) = \sum_i \Phi_i^4 / \left(\sum_i \Phi_i^2\right)^2$ [62]. The upper part shows the IPR of the most critical eigenvector and the lower part shows the IPR of the amplitude pattern for different values of κ used in the previous panels. The results confirm the increasing disorder as κ increases.

Similarly, it is shown in Fig. 4(j) that for the Rössler model the localization decreases with the node index, following the initial node indexing of Fig. 3(a). We avoid the linear fitting of eigenvectors because, as indicated by the dispersion relation, all the Laplacian modes are critical. Nevertheless, the figure reveals a clear trend of amplitude-phase differences, exhibiting the same decrement for increasing indices as observed in the corresponding real part of the dispersion relation. This suggests that nodes with higher real parts of the critical eigenvalues, λ_α, are more significantly disturbed than those with lower values. Considering that the nodes are ordered according to decreasing degree, this explains why in Fig. 1(b) the disorder is localized in the hubs of the network, a phenomenon already observed in other settings [77].

A. Amplitude-phase chimera states in other synthetic and real-world networks

In this part, we extend and validate our results by providing further evidence that localized (chaotic) disordered oscillatory patterns are also possible in other network topologies, such as Erdős-Rényi (ER) and small-world (SW) networks as demonstrated in Figure 5 (see Appendix for details on network generation). The randomness of the connections in these structures leads to the localization of the eigenvectors within a subset of nodes, similar to what has been presented so far. As a consequence, amplitude and phase chimera patterns are also observed in these topologies. Our approach is also validated for empirical networks, Figure 6, particularly

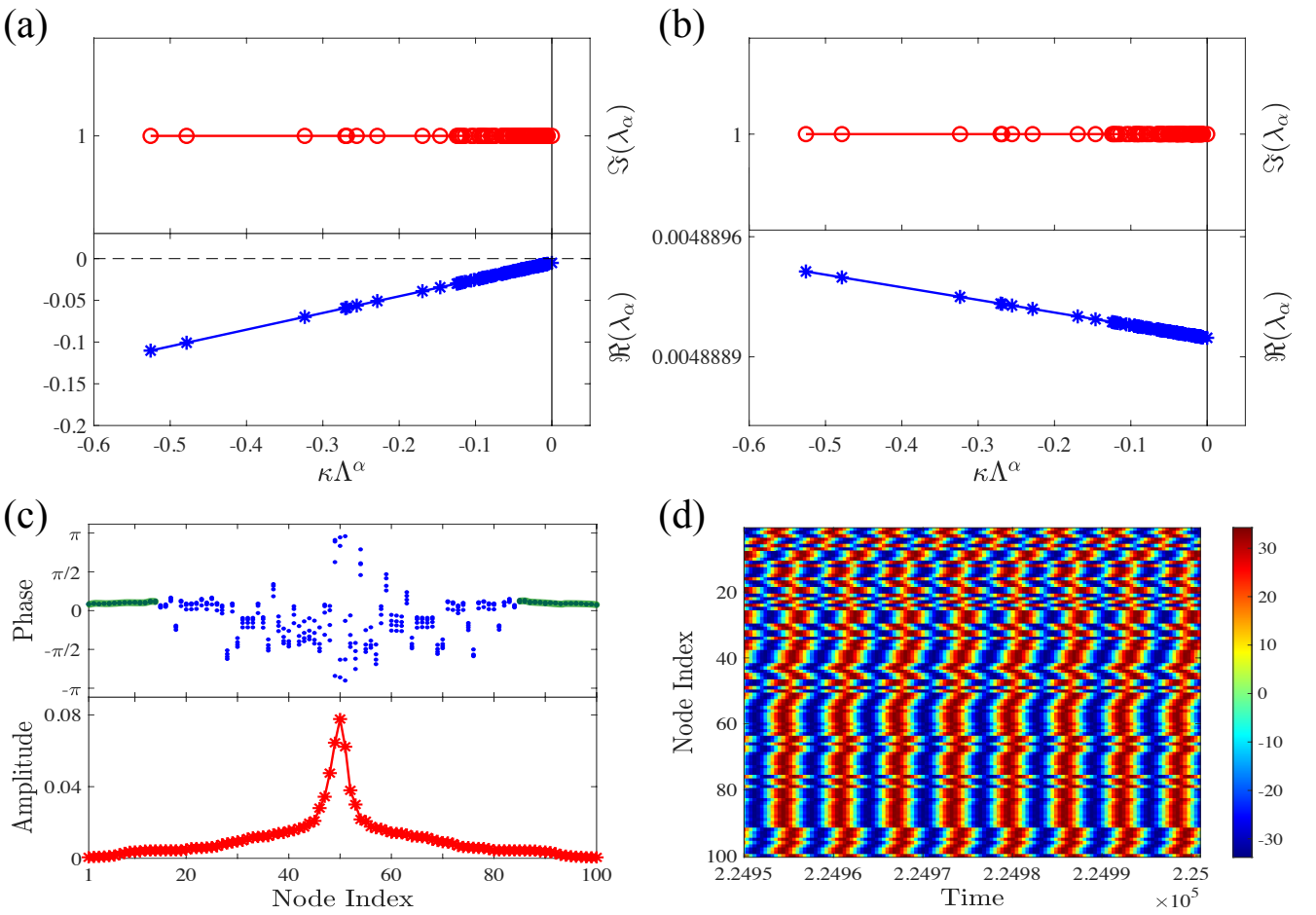

FIG. 3. **Chaotic Amplitude-Phase Chimera States in the Rössler Model.** Real (blue stars) and imaginary (red circles) parts of the dispersion relation: (a) with $a = -0.01$ and $D_\phi = D_\psi = 0.2$ in the pre-perturbation setting and (b) with $a = 0.01$ and $D_\phi = D_\psi = 0$ where chimera occurs, zoomed at the origin for clarity. (c) Stroboscopic analysis of phase differences (upper) reveals chaotic, unsynchronized oscillators, with phase-synchronized ones highlighted in green. Amplitude differences (lower) show a localized pattern. In both cases, relabeling the nodes with a center-peaked symmetric distribution helps visualize the localization of amplitude and phase disorder. (d) Equilibrium pattern showing phase disruptions. The remaining parameters are $b = 0.2$, $c = 30$, $D_\chi = 0.2$, $\kappa = 0.02$, and the network used is depicted in Fig. 1.

neuronal networks, where both empirical observations of chimeras and the role of synchronization as a main functioning mechanism have been documented. By applying our method to these real-world networks, we aim to corroborate the results obtained throughout this paper, showing that the observed patterns are not only theoretically feasible but also practically significant. This validation highlights the broader applicability and robustness of our findings across different network types and underscores their relevance in understanding the complex dynamics of real-world systems.

Unlike the previous figures, which use the stroboscopic representation of the chaotic behavior of the chimera states, here we have chosen to represent the maximum difference in the phases from their mean value using error bar notation. In Fig. 5(a)-(c), we have shown the amplitude-phase localization for an ER network. It can be noticed that the amplitude, although of a magnitude negligible compared to the phase, has weaker localization, whereas the phase chimera shows similar behavior as for the scale-free case in the previous section. In Fig. 5(d)-(f), the simulation for the SW network is presented. Here, not only do the amplitude perturbations show less localization, but the phase ones also show less localization compared to the ER case. The interpretation for such a quantitative difference from the SF network can be found in the localization properties of the eigenvector, recalling that for the particular case of the Rössler model, all the modes are critical with decreasing monotonicity toward the origin respective growth rate. As before, it is more likely that the eigenvectors with lower Laplacian eigenvalues manifest more, and in fact, for the SF network, such eigenvectors are more localized in this range of the spectrum compared to the previous two scenarios we saw here.

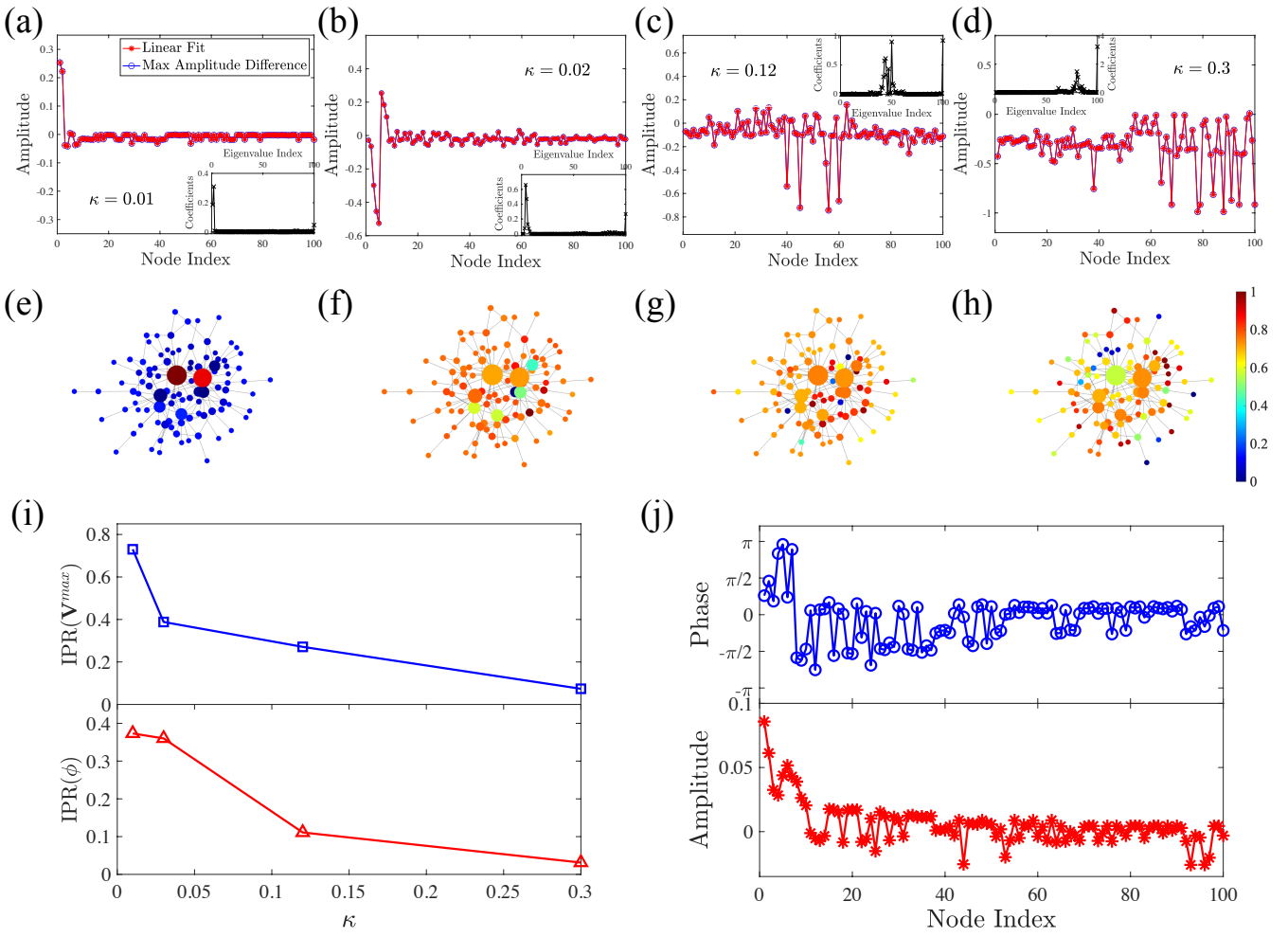

FIG. 4. **Pattern localization.** (*Brusselator*) (a)–(d) Snapshots of the final amplitude pattern with blue circles, for different values of the coupling strength κ (also specified in panel (i)). In the insets, coefficients from the linear fitting of eigenvectors, depicted as black crosses, are confirmed by the pattern's reconstruction with red stars in the main figure. (e)–(h) Network representation of the patterns above confirms the localization in nodes with similar degrees (here represented with similar size). (i) IPR calculation for the most critical Laplacian eigenvector (upper) vs. the IPR of the final patterns (lower). (*Rössler*) (j) The upper section displays phase differences from the original limit cycle (blue circles), while the lower part shows amplitude differences (red stars). The setting of parameters is as described in Fig. 2 and Fig. 3, respectively, with the only difference that D_ψ for the Brusselator is adjusted in the interval $[12.99, 13.2]$.

For the two empirical connectomes considered in Fig. 6, namely *C. elegans* (using the Brusselator model) and macaque *Rhesus brain* (using the Rössler model), the localization is overall higher across the range of the Laplacian eigenvalues, which is also reflected in the amplitude chimera localization. Notice that for the macaque connectome, the chaoticity manifests weaker than previously, and disorder in the phase has a high range but low average magnitude, a result expectable considering the marked localization of the Laplacian eigenvectors.

IV. CONCLUSIONS AND DISCUSSION

In this paper, we explored the emergence of chimera states in complex networks through the lens of pattern formation theory. On the one hand, chimera states, far from being merely mathematically elegant, play a crucial role in understanding synchronization patterns across diverse systems, from the brain to ecological networks [37, 38]. On the other hand, pattern formation theory has seen significant development in recent decades, offering insights into the formation of complex spatial patterns in both fluid and solid systems, with applications spanning physics [56] and biology [57]. Pattern formation theory, through stability analysis building on nonlinear perturbation theory, enables the prediction of patterns

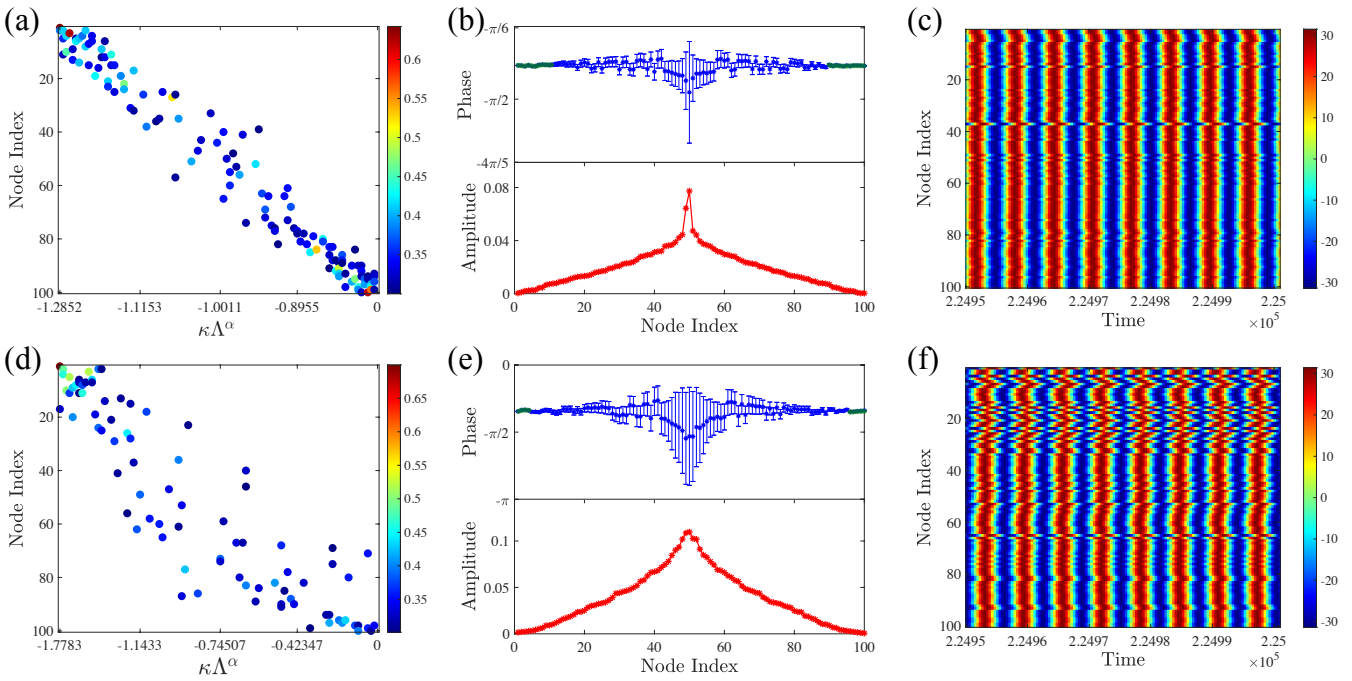

FIG. 5. **Chaotic Amplitude-Phase Chimera States in the Rössler Model for the Erdős-Rényi (upper) and Small-World (lower) networks.** Panels (a) and (d) represent the eigenvector localization, (b) and (e) show the amplitude-phase chimeras, and (c) and (f) depict the pattern evolution at equilibrium for the species ϕ, respectively. Common parameters for both cases are $a = 0.002$, $b = 0.2$, $c = 30$, $D_\phi = D_\psi = 0$, $\kappa = 0.004$. For the Erdős-Rényi network, $D_\chi = 0.5$, and we have generated a 100-node network with a wiring probability $p = 0.5$. For the small-world network, $D_\chi = 5$, and the network has 100 nodes, generated starting from a ring of $k = 4$ near neighbors and a rewiring probability $p = 0.5$.

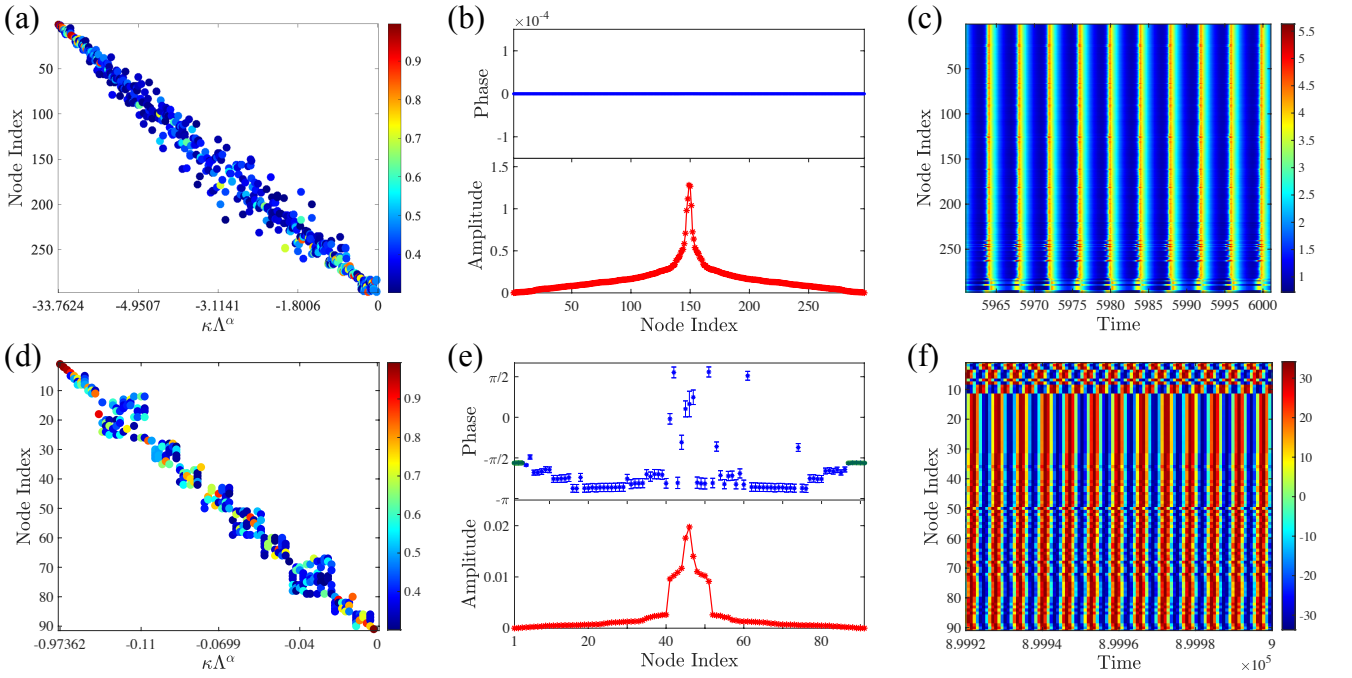

FIG. 6. **Chaotic Amplitude-Phase Chimera States in the Brusselator for the *C. elegans* (upper) and the Rössler *Rhesus macaque* (lower) neural networks.** Panels (a) and (d) represent the eigenvector localization, (b) and (e) show the amplitude-phase chimeras, and (c) and (f) depict the pattern evolution at equilibrium for the species ϕ, respectively. For the Brusselator model, the parameters are $a = 2$, $b = 5.5$, $D_\phi = 1$, $D_\psi = 2.56$, and $\kappa = 0.5$. For the Rössler model, the parameters are $a = 0.01$, $b = 0.2$, $c = 30$, $D_\phi = D_\psi = 0$, $D_\chi = 0.025$, and $\kappa = 0.02$.

in nonlinear equilibria. Since 2010, the study of Turing patterns in complex networks [67] has sparked numerous investigations into pattern formation in various network structures. Despite the advancement in pattern formation theory in networks, applications have often been constrained to specific network types such as modular [42] or non-normal ones [44], which exhibit spectral localization due to clustering or triangularization of Laplacian eigenvectors entries.

However, a general analysis of chimera state formation in complex networks has been lacking. In this manuscript, we aim to fill this gap. By leveraging the fact that many complex networks possess strongly localized eigenvectors of the Laplacian, we propose a slight destabilization of the coupled oscillator system. By tracking the propagation of this destabilization through the localized entries of the critical Laplacian eigenvector, we determine how disorder in amplitude and/or phase is induced, while synchrony is maintained in the rest of the network.

This approach provides a systematic explanation for the emergence of chimera patterns from the initial time to equilibrium, aiming in this way to fill a gap in the existing literature. While the authors acknowledge that further efforts are needed to connect the results of this paper with phase-reduced models, such as the Kuramoto model, where chimeras were originally observed and subsequently studied, they are optimistic that this proposed approach will pave the way for interesting future findings. These include exploring the multiple different chimera patterns known to exist in the literature [22], elucidating the peculiar conditions under which such states arise, and last but not least, offering tools for analyzing their stability.

ACKNOWLEDGMENTS

M.A. acknowledges support from the FSU Council on Research and Creativity SEED grant *Structure and dynamics of non-normal networks.* A.A. acknowledges support by Ministerio de Economía y Competitividad (Grants No. PID2021-128005NB-C21), European Union's Horizon Europe Programme under the CREXDATA project (grant agreement no. 101092749), Generalitat de Catalunya (Grant No. 2023PFR-URV-00633), ICREA Academia, and the Joint Appointment Program at Pacific Northwest National Laboratory (PNNL). PNNL is a multi-program national laboratory operated for the U.S. Department of Energy (DOE) by Battelle Memorial Institute under Contract No. DE-AC05-76RL01830.

APPENDIX

A. Methods

1. Details of the Linear Stability Analysis (LSA)

The linearized reaction-diffusion system is:

$$\dot{\mathbf{u}}_j = \mathbf{J}\mathbf{u}_j + \mathbf{D}\sum_{k=1}^{N} L_{jk}\mathbf{u}_k, \quad \forall j,$$

where $\mathbf{u}_j$ is the M-dimensional vector of the perturbation for the node j. We expand $\mathbf{u}_j$ in terms of the basis of eigenvectors of the Laplacian:

$$\mathbf{u}_j = \sum_{\alpha} \mathbf{c}_\alpha V_j^\alpha e^{\lambda_\alpha t},$$

where $\mathbf{c}_\alpha$ are M-dimensional vectors representing the coefficients for each species, V_j^α are the entries of the eigenvectors, and λ_α are the growth rates of the perturbations.

Substituting this expansion into the linearized reaction-diffusion equation:

$$\sum_\alpha \lambda_\alpha \mathbf{c}_\alpha V_j^\alpha e^{\lambda_\alpha t} = \mathbf{J}\sum_\alpha \mathbf{c}_\alpha V_j^\alpha e^{\lambda_\alpha t} + \\ + \mathbf{D}\sum_{k=1}^{N} L_{jk}\sum_\alpha \mathbf{c}_\alpha V_k^\alpha e^{\lambda_\alpha t}.$$

Using the property of the eigenvalues and eigenvectors of $\mathbf{L}$ we have $\sum_{k=1}^{N} L_{jk}V_k^\alpha = \Lambda^\alpha V_j^\alpha$, so we get:

$$\sum_\alpha \lambda_\alpha \mathbf{c}_\alpha V_j^\alpha e^{\lambda_\alpha t} = \mathbf{J}\sum_\alpha \mathbf{c}_\alpha V_j^\alpha e^{\lambda_\alpha t} + \\ + \mathbf{D}\sum_\alpha \Lambda^\alpha \mathbf{c}_\alpha V_j^\alpha e^{\lambda_\alpha t}.$$

Equating the terms with the same exponential factor $e^{\lambda_\alpha t}$:

$$\lambda_\alpha \mathbf{c}_\alpha V_j^\alpha = \mathbf{J}\mathbf{c}_\alpha V_j^\alpha + \mathbf{D}\Lambda^\alpha \mathbf{c}_\alpha V_j^\alpha.$$

Since this relationship must hold for each node j, and assuming that for at least one node j, $V_j^\alpha \neq 0$, we get:

$$\lambda_\alpha \mathbf{c}_\alpha = (\mathbf{J} + \Lambda^\alpha \mathbf{D})\mathbf{c}_\alpha.$$

The growth rates λ_α are the eigenvalues of the matrix $(\mathbf{J} + \Lambda^\alpha \mathbf{D})$. The dispersion relation for the growth rates λ_α as a function of the eigenvalues of the Laplacian matrix $\lambda_\alpha\,(\Lambda^\alpha)$.

2. Definitions of the Brusselator and Rössler Models

<u>Brusselator Model</u>

The Brusselator is a two-variable model of an autocatalytic reaction, and can be considered as a single, uncoupled node from a network perspective. It is described by

the following differential equations:

$$\frac{dx}{dt} = a + x^2 y - (b+1)x,$$
$$\frac{dy}{dt} = bx - x^2 y,$$

where x and y represent the concentrations of two chemical species, and a and b are constants. The fixed points of the system are given by $(x^*, y^*) = (a, b/a)$. This model exhibits a Hopf bifurcation, transitioning from a stable fixed point to a limit cycle when the parameter b exceeds the critical threshold $b_c = 1 + a^2$, indicating the onset of oscillatory behavior.

Rössler Model
The Rössler model is a three-variable system that can also be seen as a single, uncoupled node in a network context, primarily used to describe both oscillatory and chaotic dynamics. The governing differential equations are:

$$\frac{dx}{dt} = -y - z,$$
$$\frac{dy}{dt} = x + ay,$$
$$\frac{dz}{dt} = b + z(x - c),$$

with x, y, and z as the system variables, and a, b, and c as parameters. The system has two fixed points; here, we are considering the fixed point given by

$$\begin{pmatrix} x^* \\ y^* \\ z^* \end{pmatrix} = \begin{pmatrix} \dfrac{c - \sqrt{c^2 - 4ab}}{2} \\ \dfrac{-c + \sqrt{c^2 - 4ab}}{2a} \\ \dfrac{c - \sqrt{c^2 - 4ab}}{2a} \end{pmatrix}$$

The dynamics of the system undergo a significant change as a transitions from negative to positive, leading towards oscillatory and chaotic trajectories for values of c considered in the paper.

These models serve as fundamental examples of dynamical systems theory, providing insights into the behavior of chemical reactions and chaotic systems, and illustrating basic principles of oscillators within networks.

3. Network Generative Models

The synthetic networks considered in this work are undirected, unweighted, and randomly generated, as randomness is a key ingredient for the emergence of spectral localization. We focus on three well-known network models: scale-free, Erdős–Rényi, and small-world networks [1].

Scale-Free networks These are constructed using the Barabási–Albert (BA) preferential attachment model [61]. The process begins with an initial fully connected core of m_0 nodes. New nodes are added sequentially, each connecting to $m \leq m_0$ existing nodes with probability proportional to their degree. This generative rule leads to a heavy-tailed degree distribution characteristic of scale-free topologies.

Erdős–Rényi networks These are generated using the Gilbert model, in which each possible edge between N nodes is included independently with a fixed probability p [78]. This results in a binomial degree distribution and provides a homogeneous random graph structure that serves as a useful benchmark for comparison.

Small-World networks These are generated using the Watts–Strogatz algorithm [79]. The construction starts from a regular ring lattice where each node is connected to its k nearest neighbors. Then, with probability p, each edge is randomly rewired to a new target node, introducing long-range connections that create the small-world effect. This model interpolates between regular and random structures depending on the value of p.

4. Weakly nonlinear analysis

We begin by introducing small inhomogeneous perturbations, $\mathbf{u}_j$, to the uniform equilibrium point, thereby slightly perturbing the system from its steady state, $\mathbf{x}_j = \mathbf{x}_j^* + \mathbf{u}_j$ for $j = 1, \ldots, N$. Substituting this into equations (1) and performing a Taylor expansion yields the following equation for the time evolution of $\mathbf{u}_j$:

$$\dot{\mathbf{u}}_j = \mathbf{J}\mathbf{u}_j + \mathbf{D}\sum_{k=1}^{N} L_{jk}\mathbf{u}_k + \mathcal{M}\mathbf{u}_j\mathbf{u}_j + \mathcal{N}\mathbf{u}_j\mathbf{u}_j\mathbf{u}_j + \ldots \quad (5)$$

where $\mathbf{J}$ is the Jacobian matrix evaluated at the steady state $\mathbf{x}^*$, and $\mathcal{M}\mathbf{u}_j\mathbf{u}_j$ and $\mathcal{N}\mathbf{u}_j\mathbf{u}_j\mathbf{u}_j$ represent, respectively, the second and third-order terms. Redefining $\boldsymbol{\mu}$ above the supercritical Hopf bifurcation as $\boldsymbol{\mu} = \boldsymbol{\mu}_0 + \epsilon^2\boldsymbol{\mu}_1$, where $\boldsymbol{\mu}_1$ is order one and introducing a slow time variable $\tau = \epsilon^2 t$, the total derivative with respect to the original time t is then: $d/dt \longrightarrow \partial/\partial t + \epsilon^2\partial/\partial\tau$. Under the crucially imposed condition $\kappa = \epsilon^2$, the impact of diffusion is comparable to the deviation from the bifurcation point. In proximity to criticality, matrices $\mathbf{J}$ and operators $\mathcal{M}$, $\mathcal{N}$ can be expanded in powers of ϵ^2: $\mathbf{J} = \mathbf{J}_0 + \epsilon^2\mathbf{J}_1 + \ldots$, $\mathcal{M} = \mathcal{M}_0 + \epsilon^2\mathcal{M}_1 + \ldots$, and $\mathcal{N} = \mathcal{N}_0 + \epsilon^2\mathcal{N}_1 + \ldots$. Expanding $\mathbf{u}$ as a series in terms of both t and τ: $\mathbf{u}_j(t) = \sum_{n=1}^{\infty}\epsilon^n\mathbf{u}_j^{(n)}(t,\tau)$, and substituting this expansion along with the previous ones into

Eq. (5) and grouping terms by order in ϵ yields the following set of equations.

$$\left(\frac{\partial}{\partial t}\mathbb{I} - \mathbf{J}_0\right)\mathbf{u}_j^{(\nu)} = \mathbf{B}_j^{(\nu)} \tag{6}$$

for $\nu = 1, 2, 3...$ where $\mathbb{I}$ is the identity matrix and with $\mathbf{B}_j^{(\nu)}$ defined according to the superscript ν. As shown in [53, 55], the solvability condition for the linear system above, as per the Fredholm theorem, is directly satisfied for $\nu = 1$ and $\nu = 2$, while it must be explicitly imposed for $\nu = 3$. In particular, for $\nu = 1$, one has $\mathbf{B}_j^{(1)} = 0$, corresponding to the linear problem for the fast variable t with a solution

$$\mathbf{u}_j^{(1)}(t,\tau) = W_j(\tau)\mathbf{U}_0 e^{i\omega_0 t} + \text{c.c.}, \tag{7}$$

where $\mathbf{U}_0$ is the right eigenvector of $\mathbf{J}_0$ corresponding to the eigenvalue $i\omega_0$. Here $i\omega_0$ is the intrinsic frequency of the identical oscillators and c.c. stands for the complex conjugate of the preceding term. The complex variable $W_j(\tau)$ represents the amplitude of the perturbation, and its dynamics are assumed to be slow, governed by the slow time scale τ. This choice is based on the fact that when the system is very close to the threshold and on the unstable side, the growth rate causes a slow increase in amplitude, supporting the consideration of two-time-scale dynamics. For $\nu = 2$ instead, we obtain $\mathbf{B}_j^{(2)} = \mathcal{M}_0\mathbf{u}_j^{(1)}\mathbf{u}_j^{(1)}$. Next, we attempt to represent the solution of the linear system as follows:

$$\mathbf{u}_j^{(2)} = W_j^2\mathbf{V}_2 e^{2i\omega_0 t} + \gamma\mathbf{u}_j^{(1)} + |W_j|^2\mathbf{V}_0\,,$$

for some undetermined constant γ. Substituting this ansatz into (6) and collecting terms independent of t, we derive $\mathbf{V}_0 = -2\mathbf{J}_0^{-1}\mathcal{M}_0\mathbf{U}_0\mathbf{U}_0^*$, where the bar indicates the complex conjugate. Similarly, by grouping the terms proportional to $e^{2i\omega_0 t}$, we find $\mathbf{V}_2 = (2i\omega_0\mathbb{I} - \mathbf{J}_0)^{-1}\mathcal{M}_0\mathbf{U}_0\mathbf{U}_0$.

The third term in Eq. (6) is given by $\mathbf{B}_j^{(3)} = (\mathbf{J}_1 - d/d\tau\mathbb{I})\,\mathbf{u}_j^{(1)} + \mathbf{D}\sum_{k=1}^N L_{jk}\mathbf{u}_k^{(1)} + 2\mathcal{M}_0\mathbf{u}_j^{(1)}\mathbf{u}_j^{(2)} + \mathcal{N}_0\mathbf{u}_j^{(1)}\mathbf{u}_j^{(1)}\mathbf{u}_j^{(1)}$. Now, by explicitly imposing the solvability condition for $\nu = 3$, an amplitude equation for the time evolution of $W_j(\tau)$ is obtained [53, 55], also known as the Complex Ginzburg-Landau (CGL) equation

$$\frac{d}{d\tau}W_j(\tau) = \sigma W_j - g|W_j|^2 W_j + d\sum_{k=1}^N L_{jk}W_k \tag{8}$$

where the complex coefficients are given as $\sigma = \sigma_{Re} + i\sigma_{Im} = (\mathbf{U}_0^*)^T\mathbf{J}_1\mathbf{U}_0$, $d = d_{Re} + id_{Im} = (\mathbf{U}_0^*)^T\mathbf{D}\mathbf{U}_0$, and $g = g_{Re} + ig_{Im} = -(\mathbf{U}_0^*)^\dagger\left[2\mathcal{M}_0\mathbf{V}_2\mathbf{U}_0^* + 2\mathcal{M}_0\mathbf{V}_0\mathbf{U}_0 + 3\mathcal{N}_0\mathbf{U}_0\mathbf{U}_0\mathbf{U}_0^*\right]$ where $\dagger$ indicates the conjugate transpose. Here $\mathbf{U}_0^*$ is the complex conjugate of $\mathbf{U}_0$. From here, one can immediately notice the absence of dependence of the CGL coefficients on network topology. The Complex Ginzburg-Landau (CGL) equation serves as a normal form for describing the amplitude of a pattern. In the context of diffusion on one-dimensional continuous support, where $\mathbf{L}$ is replaced by $\partial^2/\partial x^2$, the CGL solution manifests as a traveling plane wave, dictating the (slow) spatial modulation of the oscillatory pattern.

5. *The solvability condition*

Fredholm theorem states that the linear equation $\mathbf{A}\mathbf{u}(t) = \mathbf{b}(t)$ is solvable if $\langle\mathbf{v}(t), \mathbf{b}(t)\rangle = 0$ for each vector $\mathbf{v}(t)$ that satisfies $\mathbf{A}^*\mathbf{v}(t) = 0$. Here, $\mathbf{A}$ denotes a linear operator, with $\mathbf{u}(t)$ and $\mathbf{b}(t)$ as complex vectors of equivalent dimensions. The adjoint operator $\mathbf{A}^*$ is defined such that $\langle\mathbf{A}^*\mathbf{y}, \mathbf{x}\rangle = \langle\mathbf{y}, \mathbf{A}\mathbf{x}\rangle$ for any vectors $\mathbf{x}$ and $\mathbf{y}$. The scalar product is defined as

$$\langle\mathbf{v}(t), \mathbf{b}(t)\rangle = \int_0^{2\pi/\omega_0} \mathbf{v}^\dagger(t)\mathbf{b}(t)dt.$$

Referring to equation (6), the Fredholm theorem first necessitates identifying $\mathbf{v}(t)$ such that $(\partial/\partial t\mathbb{I} - \mathbf{J}_0)^*\mathbf{v}(t) = 0$. Considering that $\mathbf{J}_0$ is a real matrix, integration by parts reveals that

$$\left(\frac{\partial\mathbb{I}}{\partial t} - \mathbf{J}_0\right)^* = -\left(\frac{\partial\mathbb{I}}{\partial t} + \mathbf{J}_0\right)^T.$$

Thus, the equation becomes $-(\partial/\partial t\mathbb{I} + \mathbf{J}_0)^T\mathbf{v}(t) = 0$. Following the same discussion in the main text, we seek $\mathbf{v}(t)$ in the form $\mathbf{U}_0^* e^{i\omega_0 t}$ for a specific vector $\mathbf{U}_0^*$. Substituting this ansatz results in $(\mathbf{J}_0)^T\mathbf{U}_0^* = -i\omega_0\mathbf{U}_0^*$. It is common to normalize $\mathbf{U}_0^*$ such that $(\mathbf{U}_0^*)^\dagger\mathbf{U}_0 = 1$, which facilitates calculations. Defining $\mathbf{U}_0^*$ allows us to articulate the solvability condition $\langle\mathbf{U}_0^* e^{i\omega_0 t}, \mathbf{B}_j^{(\nu)}(t,\tau)\rangle = 0$. The expressions $\mathbf{B}_j^{(\nu)}(t,\tau)$ prove to be periodic functions with a period of $2\pi/\omega_0$, they are expressed as $\mathbf{B}_j^{(\nu)}(t,\tau) = \sum_{l=-\infty}^{+\infty}\left(\mathbf{B}_j^{(\nu)}(\tau)\right)_l e^{il\omega_0 t}$. When this series is multiplied by $(\mathbf{U}_0^* e^{i\omega_0 t})^\dagger$, it results in periodic functions that, integrated over $2\pi/\omega_0$, result in zero except when $l = 1$. This leads to

$$\langle\mathbf{U}_0^* e^{i\omega_0 t}, \left(\mathbf{B}_j^{(\nu)}(\tau)\right)_1 e^{i\omega_0 t}\rangle = \int_0^{2\pi/\omega_0} (\mathbf{U}_0^*)^\dagger\left(\mathbf{B}_j^{(\nu)}(\tau)\right)_1 dt.$$

Since the integral results in zero only if the integrand is identically zero, the solvability condition simplifies to $(\mathbf{U}_0^*)^\dagger\left(\mathbf{B}_j^{(\nu)}(\tau)\right)_1 = 0\ \forall j$ and for all ν.

6. *Calculation of the CGL coefficients for the Rössler model*

In this section, we provide the calculations for a specific parameter set in the original Rössler model, with

the goal of determining the CGL equation coefficients. We begin by evaluating the Jacobian matrix at its fixed point, before perturbation, as given above.

$$\mathbf{J}_0 = \begin{pmatrix} 0 & -1 & -1 \\ 1 & a & 0 \\ \dfrac{c-\sqrt{c^2-4ab}}{2} & 0 & \dfrac{c-\sqrt{c^2-4ab}}{2} \end{pmatrix}$$

Since carrying on analytical calculations yields lengthy and not understandable formulae, we will proceed numerically considering the parameters as in the main text: $a = -0.01$, $b = 0.2$ and $c = 30$, which gives

$$\mathbf{J}_0 = \begin{pmatrix} 0 & -1 & -1 \\ 1 & -0.01 & 0 \\ -0.00007 & 0 & -0.00007 \end{pmatrix}$$

The eigenvalue we consider is $\lambda_c \approx -0.005 \pm i$, which doesn't have exactly a zero part because a is not exactly zero. If so, then the fixed point would diverge. However, its real part can be considered negligible at this level. The corresponding right and left eigenvectors are

$$\mathbf{U}_0 = \begin{pmatrix} 0.00354 + 0.70709i \\ 0.70712 \\ -0.00005 \end{pmatrix} \quad \mathbf{U}_0^* = \begin{pmatrix} 0.00349 + 0.70713i \\ 0.70712 - 0.00702i \\ 0.70716 \end{pmatrix}$$

Now let's calculate $\mathbf{J}_1$

$$\mathbf{J}_1 = \begin{pmatrix} 0 & 0 & 0 \\ 0 & 1 & 0 \\ 0.0067 & 0 & 0.0067 \end{pmatrix}$$

and recalling that $\sigma = (\mathbf{U}_0^*)^T \mathbf{J}_1 \mathbf{U}_0 = 0.5 + 0.0083i$ where clearly $\sigma_{\mathrm{Re}} > 0$. We can use the same eigenvectors to calculate $d = (\mathbf{U}_0^*)^T \mathbf{D} \mathbf{U}_0 = 0.2$ recalling that $D_\phi = D_\psi = D_\chi = 0.2$. The remaining coefficient is more involved and is given as

$$g = -(\mathbf{U}_0^*)^\dagger \left[2\mathcal{M}_0 \mathbf{V}_2 \mathbf{U}_0^* + 2\mathcal{M}_0 \mathbf{V}_0 \mathbf{U}_0 + 3\mathcal{N}_0 \mathbf{U}_0 \mathbf{U}_0 \mathbf{U}_0^*\right]$$

We recall that the second and third order terms here are defined as

$$(\mathcal{M}\mathbf{u}_j\mathbf{u}_j)_l = \frac{1}{2!} \sum_{m,n=1}^{3} \frac{\partial^2 F_l(\mathbf{x}^*, \boldsymbol{\mu})}{\partial x_n \partial x_m} (\mathbf{u}_j)_m (\mathbf{u}_j)_n$$

$$(\mathcal{N}\mathbf{u}_j\mathbf{u}_j\mathbf{u}_j)_l = \frac{1}{3!} \sum_{m,n,p=1}^{3} \frac{\partial^3 F_l(\mathbf{x}^*, \boldsymbol{\mu})}{\partial x_n \partial x_m \partial x_p} (\mathbf{u}_j)_m (\mathbf{u}_j)_n (\mathbf{u}_j)_p$$

Thanks to the dominance of linear terms in the Rössler model, the third order derivatives vanish and thus $(\mathcal{N}\mathbf{u}_j\mathbf{u}_j\mathbf{u}_j)_l = 0, \ \forall l$ independently of the choice of the vector $\mathbf{u}_j$. Due to the same property of the model, we have that only the third equation contributes to the second order term $(\mathcal{M}\mathbf{u}\mathbf{v})_3 = \dfrac{1}{2!}\left[(\mathbf{u})_1(\mathbf{v})_3 + (\mathbf{u})_3(\mathbf{v})_1\right]$ where to make the notation less confusing and ready to be used in the formula for calculating g, we have considered two different 3-dimensional vectors $\mathbf{u}, \mathbf{v}$. Now referring to [53, 55], we define $\mathbf{V}_0 = -2\mathbf{J}_0^{-1}\mathcal{M}_0\mathbf{U}_0\mathbf{U}_0^*$ and $\mathbf{V}_2 = (2i\omega_0\mathbb{I} - \mathbf{J}_0)^{-1}\mathcal{M}_0\mathbf{U}_0\mathbf{U}_0$ where $\mathcal{M}_0$ means that the operator as defined above should be evaluated at $\boldsymbol{\mu}_0$, but in our case this is not relevant since the one partial derivative involved is just a constant. Consequently

$$\mathbf{V}_0 = -2\mathbf{J}_0{}^{-1}\mathcal{M}_0\mathbf{U}_0\mathbf{U}_0^* = \begin{pmatrix} 5.1082 \times 10^{-5} \\ 5.1082 \times 10^{-3} \\ -5.1082 \times 10^{-3} \end{pmatrix}$$

$$\begin{aligned} \mathbf{V}_2 &= (2i\omega_0\mathbb{I} - \mathbf{J}_0)^{-1}\mathcal{M}_0\mathbf{U}_0\mathbf{U}_0 \\ &= \begin{pmatrix} -3.8946 \times 10^{-8} - 1.1785 \times 10^{-5}i \\ -5.8922 \times 10^{-6} - 9.98811 \times 10^{-9}i \\ -1.7677 \times 10^{-5} + 8.788 \times 10^{-8}i \end{pmatrix} \end{aligned}$$

Proceeding similarly, we finally obtain $g = 1.279 \times 10^{-5} + 0.00255i$. Most importantly, we verified that $g_{\mathrm{Re}} > 0$, indicating that the bifurcation is supercritical. The small value of g is due to the very weak linearity of the Rössler model and the third entry of the vector $\mathbf{U}_0$ which is very small.

B. Non-chaotic amplitude mediated chimera patterns

Unlike the Rössler model, the Brusselator is characterized by only two variables and, being a two-dimensional system, it cannot produce chaotic behavior according to the Poincaré-Bendixson theorem [80]. Furthermore, as discussed in the main text, the two-dimensionality of the model prevents it from undergoing a Hopf bifurcation in a non-zero spatial domain. Thus, the phase differences from the original limit cycle will always be zero. To observe non-chaotic yet oscillatory behavior in the phase difference, we consider the Rössler equations in a regime where chaos is absent, specifically for a parameter value of c lower than previously analyzed. Figure 7 illustrates this scenario (for the species ϕ), where we particularly emphasize the use of stroboscopic plotting at the same frequency as the original limit cycle. Despite apparent disorder in both amplitude and phase, no quasiperiodicity is present.

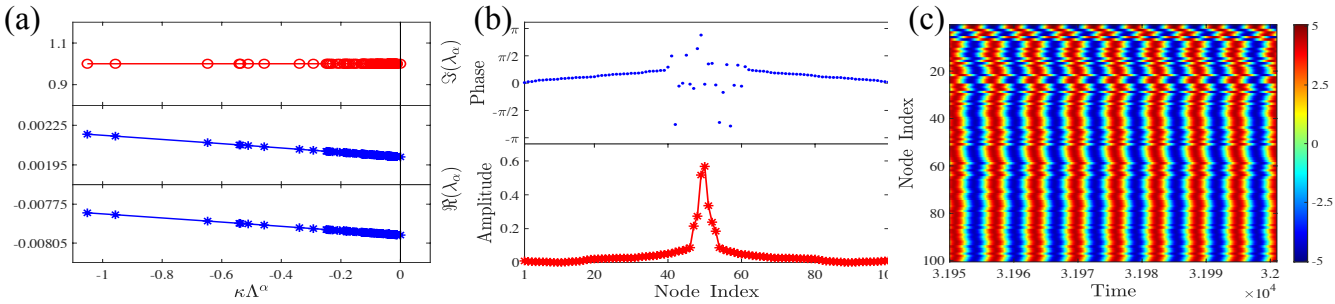

FIG. 7. **Non-chaotic Amplitude-Phase Chimera States in the Rössler Model for the species ϕ.** (a) Real (blue stars) and imaginary (red circles) parts of the dispersion relation for $a = -0.01$ (lower) and $a = 0.01$ (middle) respectively. (b) Phase differences (upper) reveal chimera states, with indices scattered for disordered patterns; amplitude differences (lower) show localized disorder, with nodes arranged for a center-peaked symmetric amplitude distribution. (c) Pattern evolution at equilibrium with visible amplitude disruptions. The rest of the parameters are $b = 0.2$, $c = 5.7$, $D_\phi = D_\psi = 0$, $D_\chi = 0.35$, and $\kappa = 0.04$, and the network used is depicted in Fig. 1.

[1] M. Newman, *Networks: An Introduction* (Oxford university press, 2010).

[2] Y. Kuramoto, Self-entrainment of a population of coupled non-linear oscillators, in *International Symposium on Mathematical Problems in Theoretical Physics*, edited by H. Araki (Springer Berlin Heidelberg, Berlin, Heidelberg, 1975) pp. 420–422.

[3] S. Strogatz, *Sync: The emerging science of spontaneous order* (Penguin UK, 2004).

[4] A. Pikovskij, M. Rosenblum, and J. Kurths, *Synchronization: a universal concept in nonlinear sciences* (Cambridge Univ. Press, Cambridge, 2007).

[5] A. Arenas, A. Díaz-Guilera, J. Kurths, Y. Moreno, and C. Zhou, Synchronization in complex networks, Physics Reports **469**, 93 (2008).

[6] E. M. Izhikevich, *Dynamical systems in neuroscience: the geometry of excitability and bursting*, Computational neuroscience (MIT Press, Cambridge, Mass, 2007) oCLC: ocm65400606.

[7] O. Sporns, *Networks of the brain* (MIT Press, Cambridge, Mass., 2011) oCLC: 707080478.

[8] J. Buck and E. Buck, Synchronous Fireflies, Scientific American **234**, 74 (1976).

[9] A. E. Motter, S. A. Myers, M. Anghel, and T. Nishikawa, Spontaneous synchrony in power-grid networks, Nature Physics **9**, 191 (2013).

[10] F. Sivrikaya and B. Yener, Time synchronization in sensor networks: a survey, IEEE Network **18**, 45 (2004).

[11] Y. Kuramoto and D. Battogtokh, Coexistence of coherence and incoherence in nonlocally coupled phase oscillators, Nonlinear Phenomena in Complex Systems **5**, 380 (2002).

[12] D. M. Abrams and S. H. Strogatz, Chimera states for coupled oscillators, Phys. Rev. Lett. **93**, 174102 (2004).

[13] M. J. Panaggio and D. M. Abrams, Chimera states: coexistence of coherence and incoherence in networks of coupled oscillators, Nonlinearity **28**, R67 (2015).

[14] A. Zakharova, M. Kapeller, and E. Schöll, Chimera death: Symmetry breaking in dynamical networks, Phys. Rev. Lett. **112**, 154101 (2014).

[15] N. Semenova, A. Zakharova, V. Anishchenko, and E. Schöll, Coherence-resonance chimeras in a network of excitable elements, Physical review letters **117**, 014102 (2016).

[16] F. P. Kemeth, S. W. Haugland, L. Schmidt, I. G. Kevrekidis, and K. Krischer, A classification scheme for chimera states, Chaos: An Interdisciplinary Journal of Nonlinear Science **26** (2016).

[17] M. J. Panaggio, D. M. Abrams, P. Ashwin, and C. R. Laing, Chimera states in networks of phase oscillators: the case of two small populations, Physical Review E **93**, 012218 (2016).

[18] T. Chouzouris, I. Omelchenko, A. Zakharova, J. Hlinka, P. Jiruska, and E. Schöll, Chimera states in brain networks: Empirical neural vs. modular fractal connectivity, Chaos: An Interdisciplinary Journal of Nonlinear Science **28**, 045112 (2018).

[19] Y. Maistrenko, S. Brezetsky, P. Jaros, R. Levchenko, and T. Kapitaniak, Smallest chimera states, Physical Review E **95**, 010203 (2017).

[20] M. Thoubaan and P. Ashwin, Existence and stability of chimera states in a minimal system of phase oscillators, Chaos: An Interdisciplinary Journal of Nonlinear Science **28** (2018).

[21] O. E. Omel'chenko, The mathematics behind chimera states, Nonlinearity **31**, R121 (2018).

[22] A. Zakharova, *Chimera patterns in networks: interplay between dynamics, structure, noise, and delay*, Understanding complex systems (Springer, Cham, 2020).

[23] F. Parastesh, S. Jafari, H. Azarnoush, Z. Shahriari, Z. Wang, S. Boccaletti, and M. Perc, Chimeras, Physics Reports **898**, 1 (2021).

[24] O. E. Omel'chenko, Coherence–incoherence patterns in a ring of non-locally coupled phase oscillators, Nonlinearity **26**, 2469 (2013).

[25] M. Wolfrum and O. E. Omel'chenko, Chimera states are chaotic transients, Physical Review E **84**, 015201 (2011).

[26] P. Ashwin and O. Burylko, Weak chimeras in minimal networks of coupled phase oscillators, Chaos: An Interdisciplinary Journal of Nonlinear Science **25** (2015).

[27] C. Bick and P. Ashwin, Chaotic weak chimeras and their persistence in coupled populations of phase oscillators, Nonlinearity **29**, 1468 (2016).

[28] G. C. Sethia, A. Sen, and G. L. Johnston, Amplitude-mediated chimera states, Physical Review E **88**, 042917 (2013).

[29] G. C. Sethia and A. Sen, Chimera States: The Existence Criteria Revisited, Physical Review Letters **112**, 144101 (2014).

[30] Y. Zhang, Z. G. Nicolaou, J. D. Hart, R. Roy, and A. E. Motter, Critical switching in globally attractive chimeras, Physical Review X **10**, 011044 (2020).

[31] Y. Zhang and A. E. Motter, Mechanism for Strong Chimeras, Physical Review Letters **126**, 094101 (2021).

[32] M. R. Tinsley, S. Nkomo, and K. Showalter, Chimera and phase-cluster states in populations of coupled chemical oscillators, Nature Physics **8**, 662 (2012).

[33] S. Nkomo, M. R. Tinsley, and K. Showalter, Chimera States in Populations of Nonlocally Coupled Chemical Oscillators, Physical Review Letters **110**, 244102 (2013).

[34] A. M. Hagerstrom, T. E. Murphy, R. Roy, P. Hövel, I. Omelchenko, and E. Schöll, Experimental observation of chimeras in coupled-map lattices, Nature Physics **8**, 658 (2012).

[35] E. A. Martens, S. Thutupalli, A. Fourrière, and O. Hallatschek, Chimera states in mechanical oscillator networks, Proceedings of the National Academy of Sciences **110**, 10563 (2013).

[36] L. Schmidt, K. Schönleber, K. Krischer, and V. García-Morales, Coexistence of synchrony and incoherence in oscillatory media under nonlinear global coupling, Chaos: An Interdisciplinary Journal of Nonlinear Science **24**, 013102 (2014).

[37] K. Bansal, J. O. Garcia, S. H. Tompson, T. Verstynen, J. M. Vettel, and S. F. Muldoon, Cognitive chimera states in human brain networks, Science Advances **5**, eaau8535 (2019).

[38] R. Sarfati and O. Peleg, Chimera states among synchronous fireflies, Science Advances **8**, eadd6690 (2022).

[39] D. M. Abrams, R. Mirollo, S. H. Strogatz, and D. A. Wiley, Solvable Model for Chimera States of Coupled Oscil-

lators, Physical Review Letters **101**, 084103 (2008).
[40] L. M. Pecora, F. Sorrentino, A. M. Hagerstrom, T. E. Murphy, and R. Roy, Cluster synchronization and isolated desynchronization in complex networks with symmetries, Nature Communications **5**, 4079 (2014).
[41] Y. Zhang and A. E. Motter, Symmetry-Independent Stability Analysis of Synchronization Patterns, SIAM Review **62**, 817 (2020).
[42] M. Asllani, B. A. Siebert, A. Arenas, and J. P. Gleeson, Symmetry-breaking mechanism for the formation of cluster chimera patterns, Chaos: An Interdisciplinary Journal of Nonlinear Science **32**, 013107 (2022).
[43] B. A. Siebert, C. L. Hall, J. P. Gleeson, and M. Asllani, Role of modularity in self-organization dynamics in biological networks, Phys. Rev. E **102**, 052306 (2020).
[44] R. Muolo, J. D. O'Brien, T. Carletti, and M. Asllani, Persistence of chimera states and the challenge for synchronization in real-world networks, The European Physical Journal B **97**, 6 (2024).
[45] M. Asllani, R. Lambiotte, and T. Carletti, Structure and dynamical behavior of non-normal networks, Sci. Adv. **4**, eaau9403 (2018).
[46] R. Muolo, M. Asllani, D. Fanelli, P. K. Maini, and T. Carletti, Patterns of non-normality in networked systems, J. Theor. Biol. **480**, 81 (2019).
[47] G. Baggio, V. Rutten, G. Hennequin, and S. Zampieri, Efficient communication over complex dynamical networks: The role of matrix non-normality, Sci. Adv. **6**, eaba2282 (2020).
[48] S. Johnson, Digraphs are different: why directionality matters in complex systems, J. Phys. Complexity **1**, 015003 (2020).
[49] A. Padmore, M. R. Nelson, N. Chuzhanova, and J. J. Crofts, Modelling the impact of structural directionality on connectome-based models of neural activity, Journal of Complex Networks **8**, cnaa033 ((2020)).
[50] S. Pranesh, D. Jaiswal, and S. Gupta, Effect of clustering on turing instability in complex networks, Chaos **34** ((2024)).
[51] X. Luo, G. Sun, R. He, Z. Jin, J. K. K. Asamoah, Y. Xue, and L. Chang, The relationship between clustering and networked turing patterns, Chaos **34** ((2024)).
[52] Y. Kuramoto, *Chemical Oscillations, Waves, and Turbulence*, edited by H. Haken, Springer Series in Synergetics, Vol. 19 (Springer Berlin Heidelberg, Berlin, Heidelberg, 1984).
[53] H. Nakao, Complex Ginzburg-Landau equation on networks and its non-uniform dynamics, The European Physical Journal Special Topics **223**, 2411 (2014).
[54] S. Contemori, F. Di Patti, D. Fanelli, and F. Miele, Multiple-scale theory of topology-driven patterns on directed networks, Physical Review E **93**, 032317 (2016).
[55] F. Di Patti, D. Fanelli, F. Miele, and T. Carletti, Ginzburg-Landau approximation for self-sustained oscillators weakly coupled on complex directed graphs, Communications in Nonlinear Science and Numerical Simulation **56**, 447 (2018).
[56] M. Cross and H. Greenside, *Pattern formation and dynamics in nonequilibrium systems* (Cambridge University Press, Cambridge, UK ; New York, 2009) oCLC: ocn268793786.
[57] J. D. Murray, *Mathematical Biology II - Spatial Models and Biomedical Applications* (Springer-Verlag, 2008).
[58] P. N. McGraw and M. Menzinger, Laplacian spectra as a diagnostic tool for network structure and dynamics, Phys. Rev. E **77**, 031102 (2008).
[59] S. Hata and H. Nakao, Localization of Laplacian eigenvectors on random networks, Scientific Reports **7**, 1121 (2017).
[60] R. Pastor-Satorras and C. Castellano, Distinct types of eigenvector localization in networks, Scientific reports **6**, 18847 (2016).
[61] A. L. Barabási and R. Albert, Emergence of scaling in random networks, Science **286**, 509 (1999).
[62] P. W. Anderson, Absence of Diffusion in Certain Random Lattices, Physical Review **109**, 1492 (1958).
[63] R. Bell, The dynamics of disordered lattices, Reports on Progress in Physics **35**, 1315 (1972).
[64] D. J. Thouless, Electrons in disordered systems and the theory of localization, Physics Reports **13**, 93 (1974).
[65] B. Kramer and A. MacKinnon, Localization: theory and experiment, Reports on Progress in Physics **56**, 1469 (1993).
[66] A. V. Goltsev, S. N. Dorogovtsev, J. G. Oliveira, and J. F. Mendes, Localization and spreading of diseases in complex networks, Physical review letters **109**, 128702 (2012).
[67] H. Nakao and A. S. Mikhailov, Turing patterns in network-organized activator–inhibitor systems, Nature Physics **6**, 544 (2010).
[68] M. Asllani, J. D. Challenger, F. S. Pavone, L. Sacconi, and D. Fanelli, The theory of pattern formation on directed networks, Nature Communications **5**, 4517 (2014).
[69] M. Asllani, D. M. Busiello, T. Carletti, D. Fanelli, and G. Planchon, Turing patterns in multiplex networks, Physical Review E **90**, 042814 (2014).
[70] M. Asllani, D. M. Busiello, T. Carletti, D. Fanelli, and G. Planchon, Turing instabilities on Cartesian product networks, Scientific Reports **5**, 12927 (2015).
[71] N. E. Kouvaris, S. Hata, and A. D. Guilera, Pattern formation in multiplex networks, Scientific Reports **5**, 10840 (2015).
[72] J. Petit, B. Lauwens, D. Fanelli, and T. Carletti, Theory of Turing Patterns on Time Varying Networks, Physical Review Letters **119**, 148301 (2017).
[73] J. Sun, E. M. Bollt, and T. Nishikawa, Master stability functions for coupled nearly identical dynamical systems, Europhysics Letters **85**, 60011 (2009).
[74] A. Nazerian, S. Panahi, and F. Sorrentino, Synchronization in networked systems with large parameter heterogeneity, Communications Physics **6**, 253 (2023).
[75] It is worth noting that numerical studies have shown that the CGL equation can exhibit chimera states [28, 29]. This provides further evidence that, as a first-order approximation of the general reaction-diffusion system (1), chimera states can theoretically appear in any system of coupled oscillators given an appropriate choice of parameters.
[76] A. M. Turing, The chemical basis of morphogenesis, Bulletin of Mathematical Biology **52**, 153 (1990).
[77] A. Arenas, A. Diaz-Guilera, and C. J. Pérez-Vicente, Synchronization processes in complex networks, Physica D: Nonlinear Phenomena **224**, 27 (2006).
[78] E. N. Gilbert, Random graphs, The Annals of Mathematical Statistics **30**, 1141 (1959).
[79] D. J. Watts and S. H. Strogatz, Collective dynamics of 'small-world' networks, Nature 10.1038/30918 (1998).

[80] S. H. Strogatz, *Nonlinear Dynamics and Chaos: With Applications to Physics, Biology, Chemistry, and Engineering*, 2nd ed. (CRC Press, Boca Raton, FL, 2015).